© Universiti Tun Hussein Onn Malaysia Publisher's Office

IJIE

Journal homepage: http://penerbit.uthm.edu.my/ojs/index.php/ijie
ISSN : 2229-838X e-ISSN : 2600-7916

The International Journal of Integrated Engineering

Development of a 4D Digital Phantom for Cone-Beam CT (CBCT) Imaging on the Varian On-Board Imager (OBI)

Adam Tan Mohd Amin[1], Siti Salasiah Mokri[1], Rozilawati Ahmad[2], Ashrani Aizzuddin Abd Rahni[1*]

[1]Faculty of Engineering and Built Environment,
Universiti Kebangsaan Malaysia (UKM), Bangi, Selangor, 43600, MALAYSIA

[2]Faculty of Health Science,
Universiti Kebangsaan Malaysia (UKM) Medical Center, Cheras, Kuala Lumpur, 56000, MALAYSIA

*Corresponding Author

DOI: https://doi.org/10.30880/ijie.2019.11.03.010
Received 15 February 2019; Accepted 4 July 2019; Available online 3 September 2019

Abstract: Mitigating effects of respiratory motion during image guided radiotherapy (IGRT) is important especially during thoracic and abdomen scanning protocols such as cone-beam CT (CBCT) imaging. However, the lack of 'ground-truth' in validating new algorithms has always been a challenge. The objective of this study is to outline the development of a novel 4D digital phantom for simulation of respiratory motion effects during CBCT image reconstruction based on Varian On-Board Imager (OBI): Half-Fan (HF) operating mode geometry. A set of actual 4D Magnetic Resonance (MR) data was used to develop the digital phantom. Firstly, the MR data sequence was extended to mimic a standard CBCT imaging acquisition protocol. Then, the images were segmented into several organs of interest and assigned with respective CT attenuation values. Subsequently, 2D projections of the developed digital phantom were simulated using the Varian OBI geometry. A Poisson noise model was also incorporated to the projection data to realistically simulate quantum noise that is present in an actual clinical environment. Three types of projections were then reconstructed using the standard 3D Feldkamp-Davis-Kress (FDK) algorithm, projections: without noise, with noise, and with noise and reconstructed with an additional Hann filter. As validation, the reconstructed images were compared against a single-frame of the developed phantom; quantitatively, using normalized root mean squared error (NRMSE) and qualitatively, using difference images. The results indicated that the phantom managed to display a consistent trend in modeling the effects of respiratory motion on the reconstructed images. On average, the NRMSE values for all three reconstructed images within the entire field-of-view (FOV) were evaluated to be approximately 29.07±0.22%. Nonetheless, the difference images indicated a large error in areas largely affected by respiratory motion. The NRMSE of a region-of-interest (ROI) near the affected area was evaluated as 51.26% that constitute to a significant +22.19% difference.

Keywords: Digital phantom, cone-beam CT, image reconstruction, respiratory motion

1. Introduction

Managing respiratory motion is crucial in image guided radiotherapy (IGRT) [1], for instance during cone-beam CT (CBCT) imaging that usually spans up to a minute for a complete scan. Currently, most clinics adopt a static 3D CBCT image reconstruction protocol to be registered with reference 3D CT images acquired prior during treatment planning. Considered as an involuntary action where a patient would continue to breathe – either regularly and/or irregularly – even in unconscious conditions, respiratory motion affects the quality of the reconstructed images during treatment delivery.

*Corresponding author: ashrani@ukm.edu.my

Therefore, using a static 3D volume would disregard the effects of respiratory motion. Tumor cells located at areas vulnerable to this motion would inevitably endure displacement thus exposing other organs-at-risk (OAR) to unnecessary radiation dose, apart from compromising treatment accuracy.

The emergence of various digital phantoms, such as the widely used 4D XCAT phantom [2] in medical imaging have greatly aided the development of new algorithms to ensure the accuracy during IGRT, thus allowing them to be simulated prior to clinical validation. However, a main challenge still remains which is to generate a digital phantom that is able to accurately emulate the internal anatomical changes of various organs due to either respiratory and/or cardiac motion.

This paper intends to simulate the effects of respiratory motion on reconstructed CBCT images, based on the current protocols of the Varian On-Board Imager (OBI) used at UKM [3]. For this purpose, a digital 4D CBCT phantom is developed from actual 4D Magnetic Resonance (MR) data. Using the simulated phantom, 2D projections are computationally simulated and subsequently reconstructed back using the standard Feldkamp-Davis-Kress (FDK) algorithm [4]. A comparison between the reconstructed images with the phantom is analyzed and presented in the Results and Discussion section.

2. Methodology

The scope of this paper is divided into 2 main parts: (1) development of a novel 4D CBCT phantom, and (2) a CBCT simulation based on the Varian OBI: Half-Fan (HF) geometry and protocol [3].

2.1 Phantom Development

The 4D CBCT digital phantom is developed from MR images that are acquired from a volunteer on a 32-channel coil 1.5T Philips Achieva^{TM} scanner [5]. The images include the thoracic region as shown in Fig. 1, with complete respiratory cycles and a 0.7s sampling time.

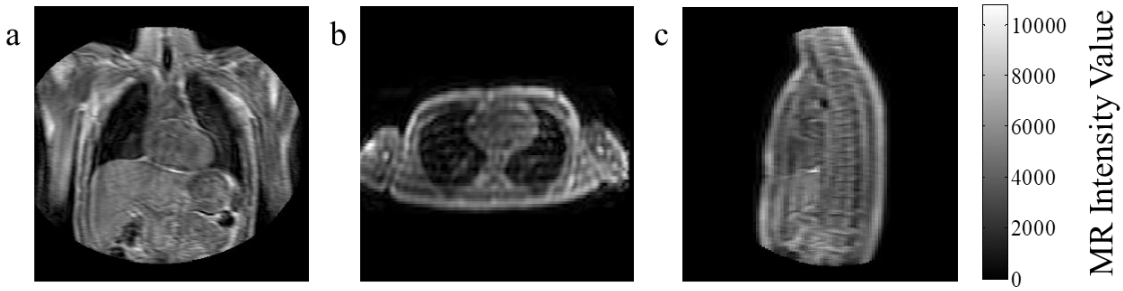

Fig. 1 – A single frame MR data across the (a) coronal, (b) axial, and (c) sagittal planes

A comparison between the parameters of the original dynamic MR data and the required CBCT specifications is shown in Table 1.

Table 1 – MR and CBCT dataset comparison

Parameters	MR	CBCT
Image size	336×45×336	384×384×64
Voxel size (mm^3)	1.482×5.5×1.482	1.172×1.172×2.5
Total length (s)	22.4	60.0
Sampling time (s)	0.7	0.0946
Total frames	35	635

The steps involved to develop the digital phantom are as shown in the flowchart shown in Fig. 2 and described in more detail in the following sub-sections.

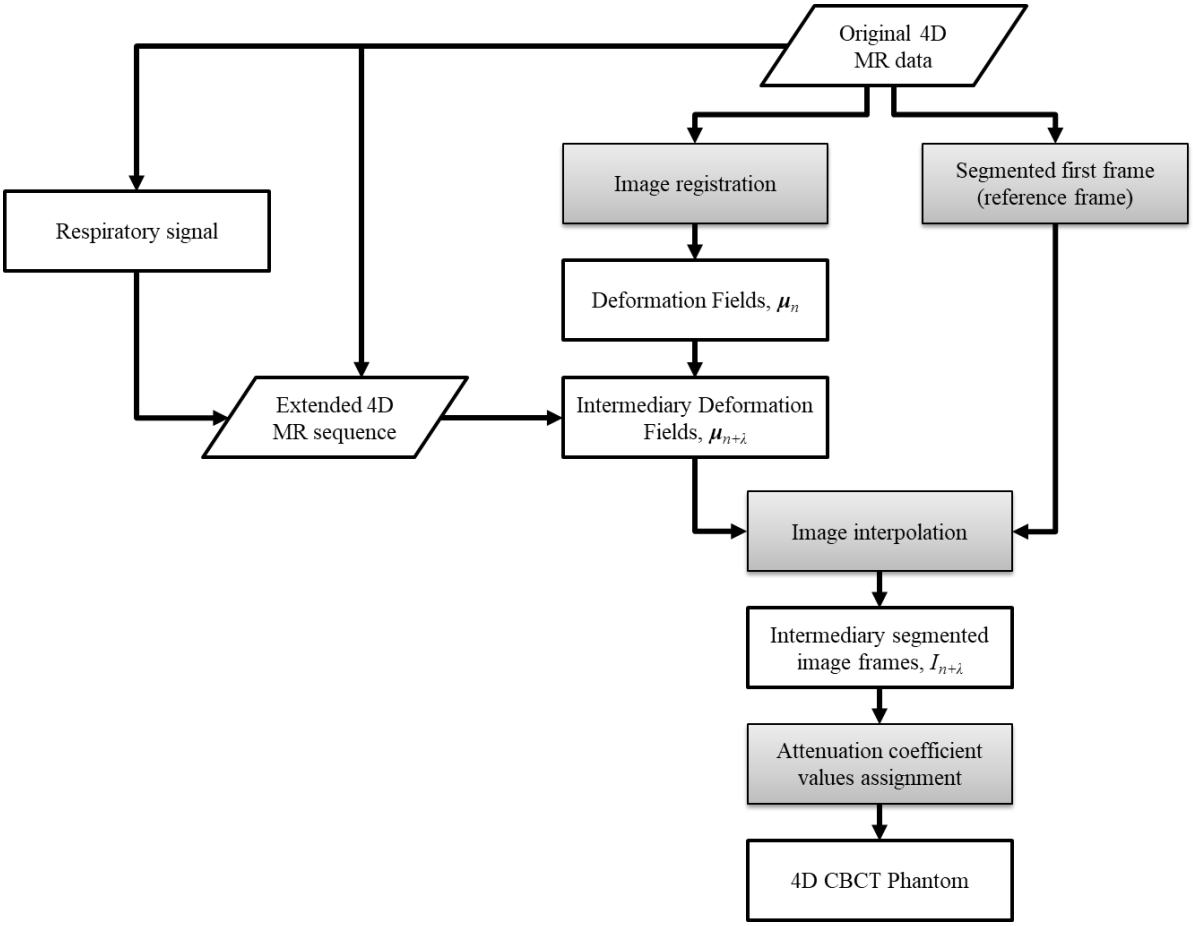

Fig. 2 – Flowchart of the 4D CBCT phantom development

2.1.1 4D MRI sequence extension

To mimic the standard 3D CBCT imaging protocol time length, the original 4D MR sequence was first extended to 1 minute. This extension is based on the respiratory signal extracted from the 4D MR sequence. The respiratory signal was extracted from the MR data by placing a virtual 'pencil-beam' identifier around a region between the right hemi-diaphragm separating the right lung and liver, as shown in Fig. 3(a). By tracing the amplitude variation of the identifier over the entire frames of the original MR data, the respiratory signal was extracted where the selected adequate-length is shown by the dotted-red-lines. Fig. 3(b) shows the extension of the original selected sequence where the dashed-blue-line marks the cut-off frame when the sequence reaches 60 seconds.

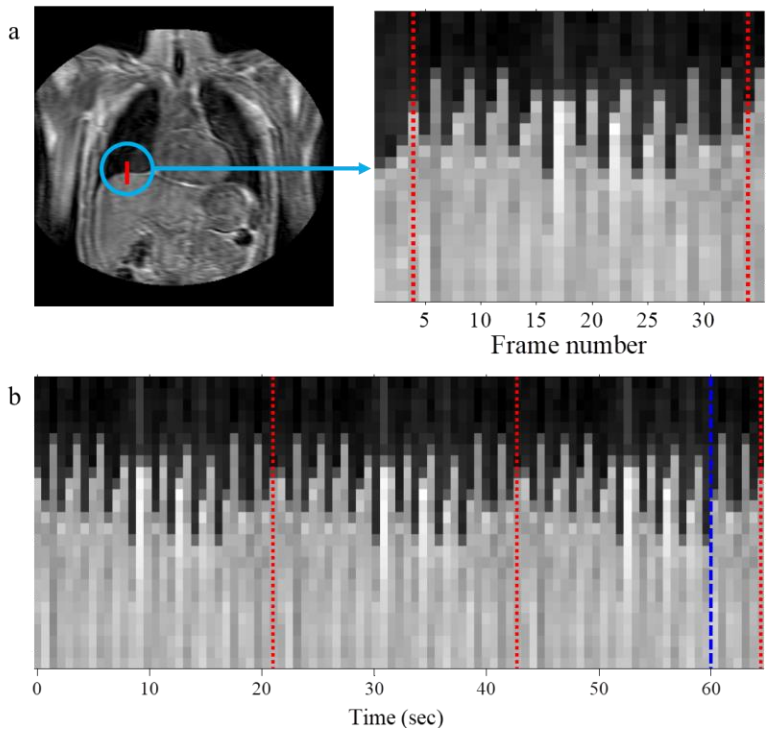

Fig. 3 – Respiratory signal (a) extraction (for frame selection), and (b) extension

2.1.2 4D MRI registration and segmentation

For a typical thoracic CBCT acquisition, approximately 635 projections are acquired by a Varian OBI over a minute, thus giving a sample time of approximately 0.0946s. As shown in Table 1, in contrast to the 0.7s MR data sampling time, additional intermediary frames are required to match the CBCT data sampling time. To generate the intermediary frames according to the CBCT sampling time, the original 4D MRI sequence is first registered to find the deformation between the first frame which is selected as the reference frame and subsequent frames. A free-form deformation scheme [8], [9] was thus used to register each 'target' frame, I_n, of the MR data with the same 'reference' frame, I_r, as shown. This generates the displacement field (DF), $\boldsymbol{\mu}_n(\mathbf{p})$, which represents the deformation of each point, $\mathbf{p}$, between frames I_r and I_n. as shown in (1).

$$I_n(\mathbf{p} + \boldsymbol{\mu}_n(\mathbf{p})) = I_r(\mathbf{p}) \quad (1)$$

On the other hand, the first image frame of the original MR sequence was also segmented into several organs of interest. In this study, vital organs that are known to be affected by respiratory motion near the thoracic region [6], namely the lungs and airway, stomach, spleen, liver, kidneys and heart, were segmented separately using the sparse field method [7]. The segmented organs are as shown in Fig. 4.

Fig. 4 – A single frame of a segmented MR data across the (a) coronal, (b) axial, and (c) sagittal planes

2.1.3 CBCT frame generation

With the original 4D MRI sequence registered, from (1), intermediary DFs, $\boldsymbol{\mu}_{n+\lambda}$, with $0 < \lambda < 1$, in between consecutive image frames, as shown in (2), can thus be generated. The required intermediary frames, $I_{n+\lambda}$, were then

interpolated according to the CBCT sampling time using (3) with the earlier segmented single frame, I_r, used as the reference frame. Fig.5 illustrates this procedure of generating the intermediary frames.

$$\mu_{n+\lambda} = \mu_n + \lambda\,(\mu_{n+1} - \mu_n) \tag{2}$$

$$I_{n+\lambda} = T_{n+\lambda}[\,I_r\,] \tag{3}$$

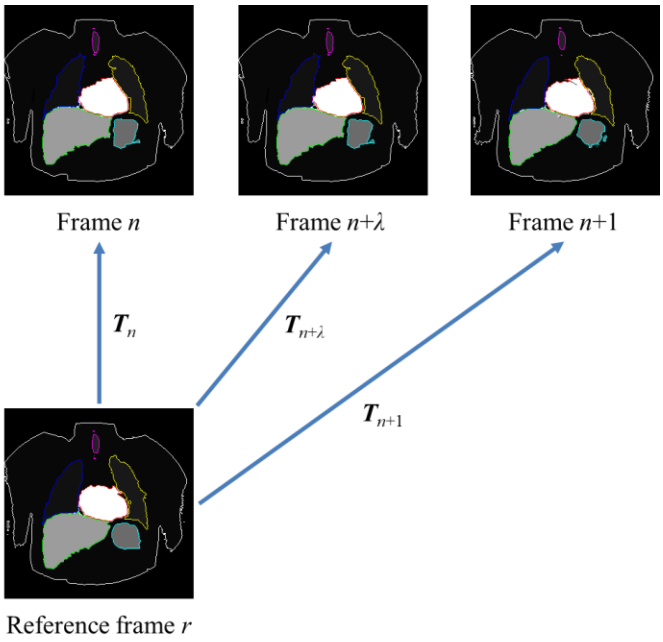

Fig. 5 – Interpolating intermediary frames

Finally, each of the organs was then assigned with their respective linear attenuation coefficient values, as shown in Table 2, to reflect the amount of radiation absorbed by the organs according to their distance from the radiation source.

Table 2 – Organs of interest and attenuation coefficient values

Organ	Attenuation Coefficient Value (mm^{-1})
Body	0.01751
Right Lung	0.005044
Left Lung	0.005044
Airways	0.01826
Stomach	0.01826
Spleen	0.01845
Liver	0.01844
Right Kidney	0.01828
Left Kidney	0.01828
Heart	0.01844

As a main characteristic of a typical CBCT image, the attenuation coefficient values are preferred compared to the standard CT Hounsfield values since the attenuation scale could enhance the contrast between each organ due to its physical characteristic of representing the radiological line integral at each image pixel [10].

2.2 Image Reconstruction

In the Varian OBI, performing CBCT within the thoracic and abdomen region requires a Half-Fan (HF) operating mode [3] to acquire 2D projections on a flat panel detector that is physically located at the opposite end against a source. Both source and detector are attached to the linear accelerator gantry via retractable robotic arms. The HF scanning mode is achieved by laterally displacing the detector and thus allowing a scan with a larger field-of-view (FOV). This is shown in axial and coronal views as shown in Fig. 6(a) and 6(b).

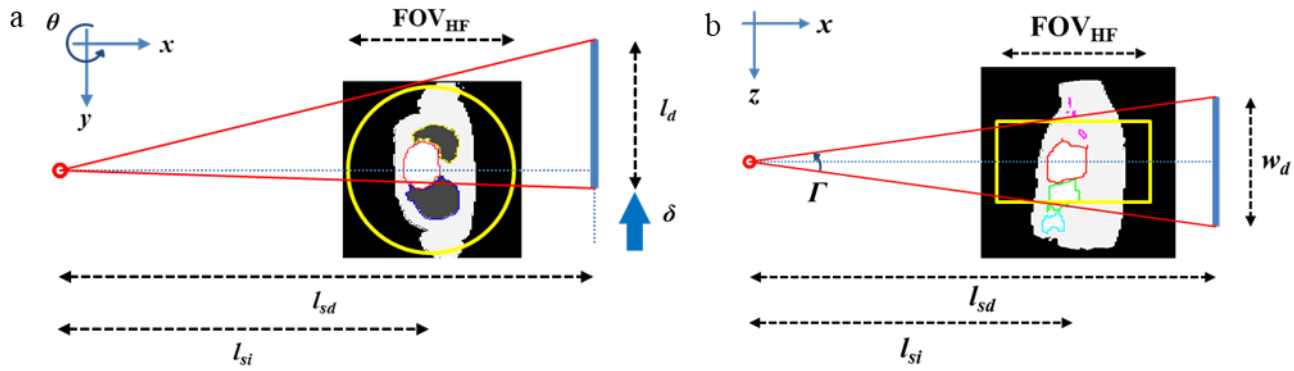

Fig. 6 – (a) Axial and (b) coronal views of the Half-Fan (HF) OBI geometry

A summary of the physical lengths used to simulate the OBI HF mode is shown in Table 3.

Table 3 – Varian OBI HF mode physical parameters

Organ	Length (mm)
Source-to-detector, l_{sd}	1500
Source-to-isocentre, l_{si}	1000
Lateral detector, l_d	397
Vertical detector, w_d	298
Lateral displacement, δ	150
HF mode FOV diameter	450
HF mode FOV length	160

With the developed CBCT phantom at the gantry isocentre, 2D HF projections, $\boldsymbol{P}$, were computed over a fully rotated $\theta = [0°, 360°]$ scan with 635 projection views. Fig. 7 shows an example of the projected phantom based on the described geometry taken at $\theta = 0°$, is shown, in which the highlighted area is the effective area of the displaced detector from the central axis, at $y = 0$ mm.

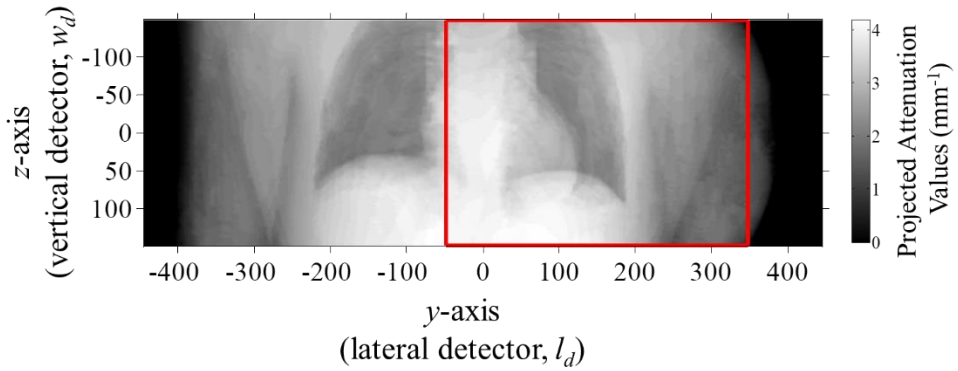

Fig. 7 – Extended 2D projection of the developed CBCT phantom

Simulated noise, $\dot{\boldsymbol{P}}$ [11] was then added to realistically model analytic imaging noise that is apparent in an actual CBCT scan. Based on the Beer-Lambert law, a noiseless transmission data, I_i, for each ray i were computed using (4), given that the mean number of incident photons for a single projection in a typical clinical study, I^0, is approximately 1.0×10^5. Assuming a negligible Gaussian-distributed electronic noise from the detector, quantum noise was modeled using a Poisson-distributed random number generator as shown in (5). A comparison between the noiseless projection data and the projection data with simulated noise on the 2D flat panel detector are shown in Fig. 8(a) and Fig. 8(b) respectively. The simulated noise model, i.e. the difference between the noiseless and projection with noise projections, is also shown in Fig. 8(c).

$$I_i = I^0 \exp(-\boldsymbol{P}_i) \tag{4}$$

$$\dot{\boldsymbol{P}}_i = \log(I^0 / \text{Poisson}(I_i)) \tag{5}$$

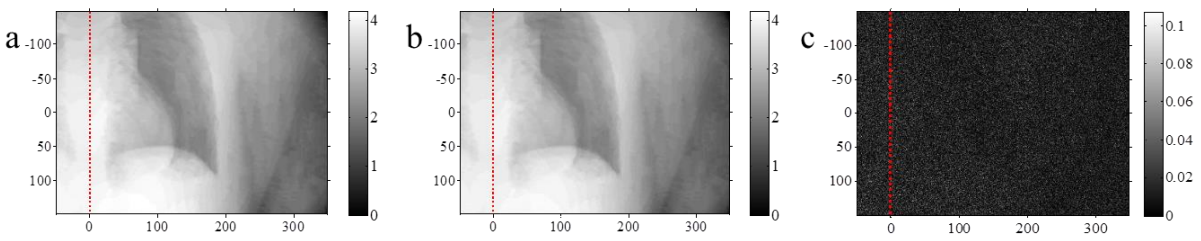

Fig. 8 – Projections: (a) without noise, and (b) with noise, using the (c) simulated Poisson noise model

In this study, the standard 3D Feldkamp-Davis-Kress (FDK) algorithm [4] was used to reconstruct the images from all of the projection views. The algorithm uses a heuristic to approximate the reconstruction based on the Filtered Back-Projection (FBP) algorithm of each axial slice along the cone-angle, Γ, as shown in Fig. 6(b). An additional Hann filter [12] was applied on-top of the standard Ram-Lak filter to the simulated noisy projected data, $\dot{\boldsymbol{P}}$ to mitigate the noise effect prior to the backprojection step in FBP.

The 3D reconstructed image was evaluated against a single-frame developed phantom taken at the end-expiration phase, as shown in Fig. 9. Highlighted in the figures is the reconstruction FOVs of the standard Varian OBI: HF CBCT reconstruction protocol as mentioned in Table 3 prior.

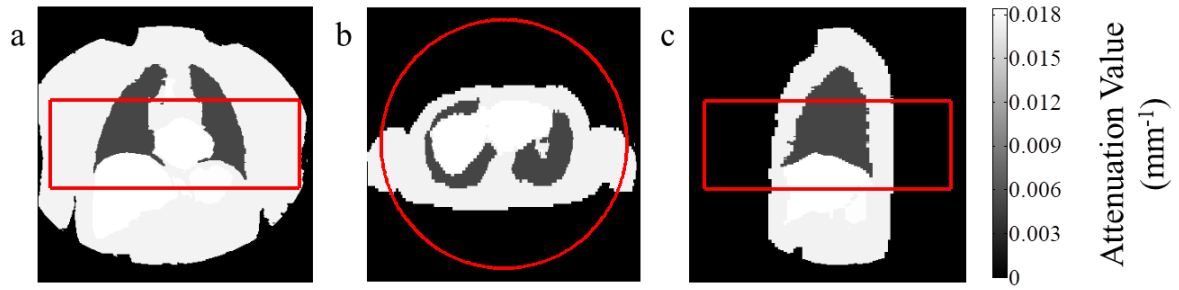

Fig. 9 – Developed phantom with reconstruction FOV across the (a) coronal, (b) axial, and (c) sagittal planes

The evaluation was done qualitatively by taking the difference image between the original single-frame phantom, I^P, with the reconstructed 3D image, I^R, and quantitatively using the normalized root mean squared error (NRMSE) [3] as shown in (6), where $m = 1, 2 \ldots M$ with M being the total number of voxel elements within the reconstructed FOV.

$$NRMSE = \frac{1}{\max(I^P) - \min(I^P)} \sqrt{\frac{\sum_{m=1}^{M} \left(I_m^P - I_m^R\right)^2}{M}} \qquad (6)$$

3. Results and Discussion

3.1 4D CBCT digital phantom

The approach of generating the segmented 4D MR data used in this study is similar to the described framework of generating a segmented 4D MR data sequence by just transforming a single static MR image using the deformation fields obtained via registration on the original MR data [5]. Although it is also possible to adopt an alternative approach by performing image segmentation on each of the image frames in the MR sequence individually, however the latter approach could contribute to a larger progression error since the deformation fields are a result of registration between the original MR data. Registering between the individually segmented MR data to obtain its corresponding deformation fields might be a way to overcome this. However, this would eventually compromise the quality of the fields prior to interpolation since registering the segmented organs omits the influence of other organs that are not included during segmentation.

Based on the extended 4D MR data sequence shown in Fig. 3(b) earlier, the large sampling time can be observed by the apparent discontinuity of the diaphragm motion in between frames. Nonetheless, using the interpolation scheme described in Fig. 5, the sampling time is reduced to match the CBCT parameters. A segmented image (as in Fig. 4) of the respiratory signal from the extended data in Fig. 3(b) is shown in Fig. 10(a). The respiratory signal of the interpolated data, as shown in Fig. 10(b), was also extracted using the same technique of placing a 'pencil-beam' identifier on the same location on each of the generated intermediary frames, $I_{n+\lambda}$, described earlier. It can be seen from both figures that

because of the low CBCT sampling time as a result of interpolation in generating the intermediary frames, the diaphragm motion was 'smoothened' in between the end-exhale (maximum peaks) and end-inhale (minimum peaks) positions, thus providing a more realistic motion for the developed digital phantom. Following the steps of developing the CBCT phantom shown in Fig. 2, a single frame of the CBCT phantom, assigned with the respective attenuation coefficient values listed in Table 2, during the end-expiration breathing phase is shown in Fig. 11.

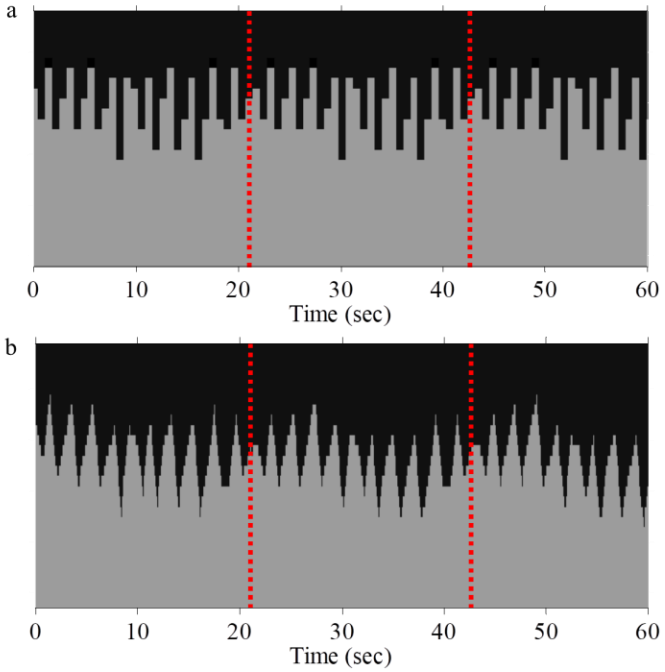

Fig. 10 – Respiratory signal extracted from (a) segmented MR data, and (b) interpolated phantom data

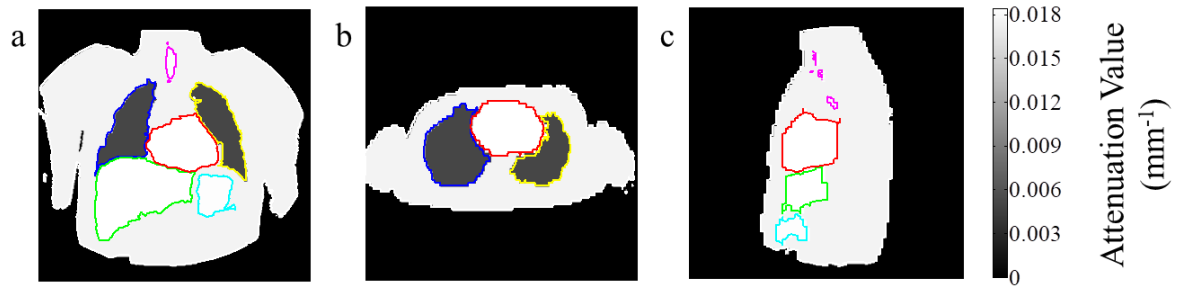

Fig. 11 – A frame of the developed CBCT phantom across the (a) coronal, (b) axial, and (c) sagittal mid-planes

3.2 Reconstructed Images

Using the FDK algorithm, the reconstructed images restricted to the Half-Fan FOV are shown in Fig. 12. Three sets of images where reconstructed from three different types of projections. A noiseless projected 4D CBCT phantom was reconstructed and shown in Fig. 12(a). Then, a projected 4D CBCT phantom that was incorporated with the quantum noise model was also reconstructed and shown in Fig. 12(b) and Fig. 12(c), with the latter having an additional Hann filter as described previously.

Based on the images, it can be seen that there is an intensity bias in intensity level on the reconstructed images when compared with the phantom shown in Fig. 9 earlier. Comparing the reconstructed attenuation coefficient values against the original phantom, the mean intensity bias is approximately ±30.06% for all three sets of reconstructed images. The reason for this intensity bias is due to the weighting factor applied to the projections required during the standard 3D FDK reconstruction algorithm used for the HF geometry, as discussed in [13]. The bias concern can be addressed by considering the mean bias when reconstructing the images, given the knowledge of the attenuation coefficient values of the digital phantom. Nonetheless, it would be impractical when implementing the algorithm clinically.

Apart from that, apparent motion artifacts can be observed in the axial plane of the reconstructed images shown in Fig. 12, when compared to the phantom in Fig. 9. Fig. 9 is a single frame of the 4D phantom at the end-exhale breathing phase. This is because the 3D reconstruction FDK algorithm that is currently used in a typical thoracic/abdomen scan protocol does not consider projection views at different breathing phases.

Quantitatively, the NRMSE values of the reconstructed images against the developed CBCT digital phantom shown in Fig. 9 are tabulated in Table 4. Observing the values across the columns, the simulated phantom displayed the desired outcomes. Comparing between the noiseless and with noise phantoms, the NRMSE values showed an increase of approximately +0.58%. Whereas with the additional Hann filter to mitigate the noise, approximately −0.50% decrease in NRMSE was achieved, i.e. only an increase of approximately +0.08% from the noiseless phantom. This shows that the simulation managed to display the effect of noise in the CBCT phantom, mimicking noise that are actually present in clinical CBCT data, while the Hann filter managed to mitigate some fraction of the noise.

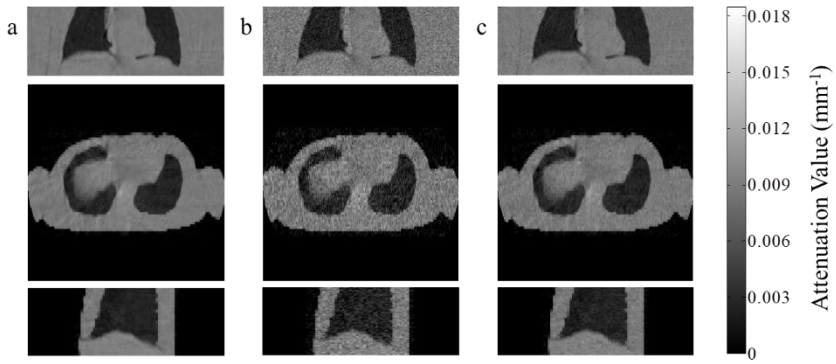

Fig. 12 – Reconstructed images on the coronal, axial and sagittal planes respectively using projections from the developed CBCT digital phantom: (a) no noise, (b) added noise, and (c) added noise with additional filter

Table 4 – MR and CBCT dataset comparison

Projection type	No Noise	+ Noise	+ Noise + Hann
NRMSE (%)	28.85	29.43	28.93

Although generally the NRMSE values are almost similar at approximately 29.07±0.22%, this is because the value is taken from the entire FOV where not all of the areas are significantly affected by motion. Contrasting the difference images as shown in Fig. 13 shows there are high differences especially around areas that are largely affected by respiratory motion e.g. diaphragm, lung walls, heart etc. As an example, consider a region of interest (ROI) as highlighted in the difference image of the reconstructed image from projections incorporated with noise and additional Hann filter as shown in Fig. 13(c). The NRMSE value within the ROI is evaluated as 51.26% that constitutes to a significant +22.19% average difference when compared to a more 'generic' NRMSE value over the entire FOV. Based at Fig. 13(d), which is an enlarged view of the ROI for the coronal plane in Fig. 13(c), the motion artifacts caused by the diaphragm movement during respiration can also be deduced by the spectrum of the difference image.

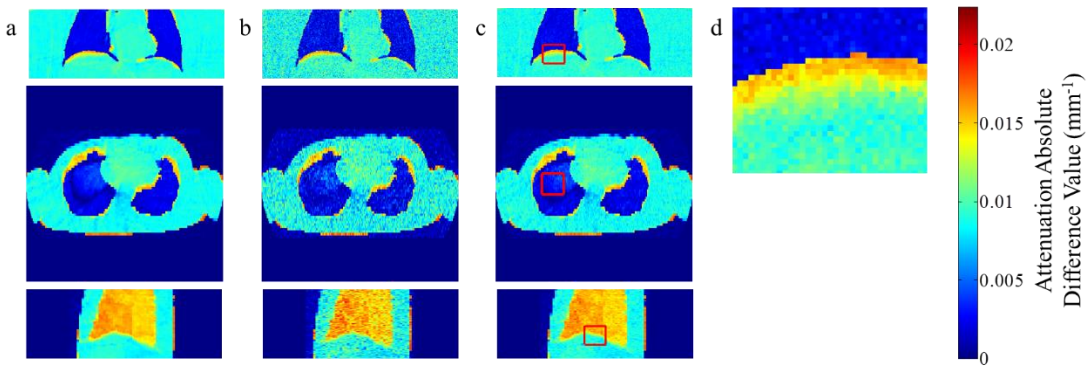

Fig. 13 – Difference images using projections: (a) without noise, (b) with noise, and (c) with noise and filter; whilst (d) enlarged view of the ROI for the coronal plane of (c)

From the results, it is shown that respiratory motion that occurs during a 1-minute CBCT scan degrades the quality of the 3D reconstructed images. Thus, the current protocol using the existing reconstruction algorithm is insufficient to accurately reconstruct an image within the thoracic and abdomen region that are largely affected by respiratory motion. Nonetheless, this analysis is only possible using a digital phantom. This is because; the advantage of utilizing a simulated phantom is the availability of a 'ground truth' to validate virtually conducted clinical experiments. This approach is preferred especially when proceeding with a clinical trial for validation is impractical and costly. Furthermore, currently

there is not a physical phantom that is able to accurately model the variability of the human respiratory motion. The advantage of using this developed 4D CBCT digital phantom over existing phantoms such as the 4D XCAT [2] phantom is that this phantom provides actual motion of each tissue and organ independently. Unlike XCAT, although it provides detailed human anatomical features and includes an internal motion model derived from 4D CT data [14], the motion model heavily depends on a user-defined motion curve that does not simulate the motion of each organ uniquely, thus hindering its ability to simulate complex deformations due to respiration [15].

4. Conclusion

In this study, a novel dynamic Cone-Beam CT (CBCT) digital phantom was successfully developed from actual 4D Magnetic Resonance (MR) data. Using this 4D digital phantom, the currently-used protocol for thoracic and abdomen CBCT imaging was virtually simulated based on the Varian On-Board Imager (OBI): Half-Fan (HF) operating mode successfully. The results suggest that respiratory motion artifact is evident in the static reconstructed images and affects image quality. Therefore, the current protocol needs to consider respiratory motion during the image reconstruction process, to ensure accuracy in Image Guided Radiotherapy Treatment (IGRT).

Acknowledgement

Adam Tan Mohd Amin is funded by MyBrain15 under Ministry of Higher Education Malaysia.

References

[1] V. Caillet, J. T. Booth, and P. Keall, "IGRT and motion management during lung SBRT delivery," Physica Medica, 2017.

[2] W. P. Segars, B. M. Tsui, J. Cai, F.-F. Yin, G. S. K. Fung, and E. Samei, "Application of the 4D XCAT Phantoms in Biomedical Imaging and Beyond," IEEE Transactions on Medical Imaging, vol. 0062, no. c, pp. 1–1, 2017.

[3] A. T. M. Amin, A. A. A. Rahni, S. S. Mokri, and R. Ahmad, "Modeling the Varian On-Board Imager (OBI): Cone-beam CT (CBCT) operating modes," Proceedings of the 2017 IEEE International Conference on Signal and Image Processing Applications, ICSIPA 2017, pp. 117-122, 2017.

[4] L. A. Feldkamp, L. C. Davis, and J. W. Kress, "Practical cone-beam algorithm," Journal of the Optical Society of America A, vol. 1, no. 6, p. 612, 1984.

[5] C. Tsoumpas, C. Buerger, A. P. King, P. Mollet, V. Keereman, S. Van-denberghe, V. Schulz, P. Schleyer, T. Schaeffter, and P. K. Marsden, "Fast generation of 4D PET-MR data from real dynamic MR acquisitions," Physics in Medicine and Biology, vol. 56, no. 20, pp. 6597-6613, 2011.

[6] P. J. Keall, G. S. Mageras, J. M. Balter, R. S. Emery, K. M. Forster, S. B. Jiang, J. M. Kapatoes, D. a. Low, M. J. Murphy, B. R. Murray, C. R. Ramsey, M. B. Van Herk, S. S. Vedam, J. W. Wong, and E. Yorke, "The management of respiratory motion in radiation oncology report of AAPM Task Group 76." Medical Physics, vol. 33, no. 10, pp. 3874–3900, 2006.

[7] S. Lankton, "Sparse Field Methods - Technical Report," Tech. Rep., 2009.

[8] S. Ourselin, R. Stefanescu, and X. Pennec, "Robust Registration of Multi-modal Images: Towards Real-Time Clinical Applications," 2002, pp. 140-147.

[9] M. Modat, G. R. Ridgway, Z. A. Taylor, M. Lehmann, J. Barnes, D. J. Hawkes, N. C. Fox, and S. Ourselin, "Fast free-form deformation using graphics processing units," Computer Methods and Programs in Biomedicine, vol. 98, no. 3, pp. 278-284, 2010.

[10] M. Chao, J. Wei, T. Li, Y. Yuan, K. E. Rosenzweig, and Y. C. Lo, "Robust breathing signal extraction from cone beam CT projections based on adaptive and global optimization techniques," Phys. Med. Biol., vol. 61, no. 8, pp. 3109–3126, 2016.

[11] Y. Liu, J. Ma, Y. Fan, and Z. Liang, "Adaptive-weighted total variation minimization for sparse data toward low-dose x-ray computed tomography image reconstruction," Physics in Medicine and Biology, vol. 57, no. 23, pp. 7923–7956, 2012.

[12] J. Fessler, "Fundamentals of CT Reconstruction in 2D and 3D", 2014.

[13] A. T. M. Amin, A. A. A. Rahni, S. S. Mokri, and R. Ahmad, "Comparison Between Projection Weighting and Rebinning Approaches in Analytical Image Reconstruction in Off-Center Flat Panel Cone-Beam CT Imaging," in 2018 2nd International Conference on BioSignal Analysis, Processing and Systems (ICBAPS), 2018, pp. 33–36.

[14] I. Vergalasova, J. Cai, W. Giles, W. P. Segars, and F. F. Yin, "Evaluation of the effect of respiratory and anatomical variables on a Fourier technique for markerless, self-sorted 4D-CBCT," Phys. Med. Biol., vol. 58, no. 20, pp. 7239–7259, 2013.

[15] X. Liu, "Optimization and Clinical Evaluation of a Prior Knowledge-based 4D Cone Beam CT Estimation Technique for Lung Radiotherapy", 2018.